Lanthanide Double Perovskite Nanocrystals with Emissions Covering the UV-C to NIR Spectral Range

Peter Saghy, Alexander M. Brown, Chun Chu, Lacie C. Dube, Weiwei Zheng, Jerome R. Robinson,* and Ou Chen*

Lead halide perovskite nanocrystals (NCs) have recently drawn considerable attention in the fields of materials science and nanotechnology. However, a major drawback of these NCs is the reliance on toxic lead, which hinders widespread application. Herein, a new class of lead-free perovskite NCs, that is, lanthanide double perovskite (Ln-DP) NCs, with f-orbital-induced optical properties, is introduced. The Pr-, Ce-, Tb-, Eu-, Sm-, and Yb-based Ln-DP NCs display narrow d→f and f→f emissions ranging from the UV-C to the near-infrared spectral region. Experimental data and calculations reveal that the emissive Ln-DP NCs exhibit small molecule-like electronic absorptions: f→d atomic transitions or ligand-to-metal charge transfer transitions. Last, it is demonstrated that by alloying Ln compositions in the DP NCs, new materials with unique and improved optical properties can be obtained. These Ln-DP NCs are promising for optical sensing and lighting, and as components in optoelectronic and/or magneto-fluorescent devices.

1. Introduction

Lead halide perovskite nanocrystals (NCs) with a chemical formula of $APbX_3$ (A: Cs^+ and methylammonium, and X: Cl^-, Br^-, or I^-) have drawn an unprecedented amount of research and technological attention owing to their superior optical and optoelectronic properties.[1] Despite extensive research efforts focusing on lead halide perovskites, their integration in potential applications has been severely burdened by lead-induced toxicity issues, raising significant environmental concerns.[2] One potential solution is to exclude lead from the perovskite-based NCs through compositional substitution.[3] In this regard, substituting every two divalent lead cations with a pair of monovalent and trivalent metal cations results in a double perovskite (DP) crystal structure with a general formula of $A_2M(I)M(III)X_6$,

P. Saghy, A. M. Brown, L. C. Dube, J. R. Robinson, O. Chen
Department of Chemistry
Brown University
324 Brook St., Providence, RI 02912, USA
E-mail: jerome_robinson@brown.edu; ouchen@brown.edu
C. Chu, W. Zheng
Department of Chemistry
Syracuse University
Syracuse, NY 13244, USA

The ORCID identification number(s) for the author(s) of this article can be found under https://doi.org/10.1002/adom.202300277

which can serve as one important alternative of lead halide perovskites.[3c,j,p,u] Such a DP crystal structure with lead exclusion can effectively reduce toxicity of the materials while preserving the original 3D cubic perovskite crystal lattice.[2b,3p,u] While alkali metals or silver are the common choices for the monovalent M(I) cation site, large main group elements such as In, Sb, and Bi have been in the center of focus occupying the trivalent M(III) cation site.[3p,4] Comparing to the transition metals, these main group elements are relatively cost-effective, less toxic, and can satisfy the tolerance factor requirement of the 3D perovskite structure.[5] Despite the lower toxicity, main group DP structures often suffer from unfavorable luminescence properties caused by their indirect bandgaps, necessitating further compositional tuning for practical applications.[3p,6]

Lanthanide (Ln; La–Lu) elements are generally considered non-toxic and can form large, air-stable trivalent Ln(III) cations. Even the rarest Lns are more abundant than the main group or transition metals frequently encountered in double perovskites (e.g., Ag, Bi, and In).[7] Owing to the presence of f-electrons, these Ln cations display unique optical and magnetic properties including narrow emission peaks with high photoluminescence (PL) quantum yields (QYs), long spin coherence lifetimes, efficient light conversion through potential quantum cutting or upconversion processes, strong magnetic responses induced by unpaired f-electrons, and broad-band X-ray scintillation behaviors.[8] While main group elements usually only enable luminescence in or near the visible spectrum, Ln ions can display narrow emission peaks ranging from deep UV to IR. These properties make the Ln-containing materials ideal for a wide range of applications, such as light emitting diodes (LEDs) and lasers, optical/temperature sensors, X-ray scintillators, magnetic resonance imaging agents, and nano-Qbits.[8b,9] Ln-containing small molecules are frequently studied for the aforementioned purposes, but they are often only stable under inert conditions. For example, $(NEt_4)_3[LnCl_6]$ small molecules—close analogs of halide perovskites—cannot be handled in ambient air for even minutes due to being extremely hydroscopic.[10] Therefore, significant research efforts have been drawn to introducing Ln elements into perovskite bulk or nanomaterials, albeit mainly as low concentration doping components for either conventional $APbX_3$ perovskite lattices or $A_2M(I)M(III)X_6$ DP NCs.[8d,9a,11]

ADVANCED
SCIENCE NEWS
www.advancedsciencenews.com

ADVANCED
OPTICAL
MATERIALS
www.advopticalmat.de

Although bulk Ln-based DP (Ln-DP) phases have been known for decades,[8b,12] their utility is limited by complicated high temperature synthesis (>900 °C) and insolubility in most solvents except for water, which is detrimental to their crystal structure. The stability of Ln-DPs can be improved by fabricating nanomaterials surrounded by hydrophobic capping ligands. For example, the recently reported $Cs_2NaErCl_6$ DP NCs were found to be stable in ambient air for at least 1 month.[13] The synthesized $Cs_2NaErCl_6$ DP NCs show near-IR (NIR) luminescence in the spectral range relevant for telecommunication. Despite the similarity of all Ln elements across the period, no other $Cs_2NaLnCl_6$ DP NCs have been reported so far.

Herein, we present a versatile colloidal method for the synthesis of $Cs_2NaLnCl_6$ DP NCs for all Lns except for lutetium and promethium. The as-synthesized Ln-DP NCs (Ln = La–Nd, Sm–Yb) display uniform size and cubic shape with a pure DP crystal phase. In addition to the already reported $Cs_2NaErCl_6$ DP NCs, we found that six additional Ln-DP NCs (Ln = Ce, Pr, Sm, Eu, Tb, and Yb) exhibit characteristic emission features covering a wide spectral window from UV-C to NIR (i.e., 260–995 nm). In particular, the $Cs_2NaPrCl_6$ DP NCs display rarely accessible UV-C emission with a PLQY of 14%, the highest QY value reported for any UV-C emitting perovskite NCs. The $Cs_2NaTbCl_6$ DP NCs show bright green emission with a PLQY of 45%, the highest value of any pure Ln-DP NCs known so far. By analyzing the optical behaviors of these materials with the aid of density functional theory (DFT) calculations, fundamental origins of the absorption and emission electronic transitions were identified and understood. Furthermore, taking advantage of high miscibility of different Lns, we have successfully demonstrated the possibility of fabricating alloyed $Cs_2NaLnCl_6$ DP NCs simultaneously containing multiple different Ln components. The resulting alloyed Ln-DP NCs possess optical properties that are inaccessible to the single Ln counterparts. Our study provides fundamental insight into electronic structure and optical properties of Ln-based perovskite materials, which will enable further development of Ln-DP NCs. The synthesized Ln-DP NCs are potentially suitable materials for a wide range of applications, including ultra-high energy LEDs, high-security anti-counterfeiting, efficient luminescent solar concentrators, as well as low-threshold lasers.

2. Results and Discussion

2.1. Synthesis, Morphology, and Crystal Phase of Ln-DP NCs

Ln-DP NCs were synthesized using a modified colloidal hot injection approach (see Supporting Information).[14] Briefly, cesium carbonate, sodium acetate, and Ln-acetate or acetylacetonate salts were added to a solution mixture of octadecene, oleic acid, and oleylamine. After oxygen and water were removed by degassing under vacuum for 1 hour at 110 °C, the solution was heated to 180 °C. Chlorotrimethylsilane was injected into the reaction solution, followed by rapid cooling to room temperature after 2 min. After purification, the obtained Ln-DP NCs can be redispersed in hexane to form a stable suspension. Powder X-ray diffraction (XRD) patterns of all the samples showed a cubic DP crystal phase (space group: Fm3m) with no indication of impurity presence (**Figure 1**A). The position of the diffraction peaks shifted systematically to higher 2θ angles moving down the Ln series
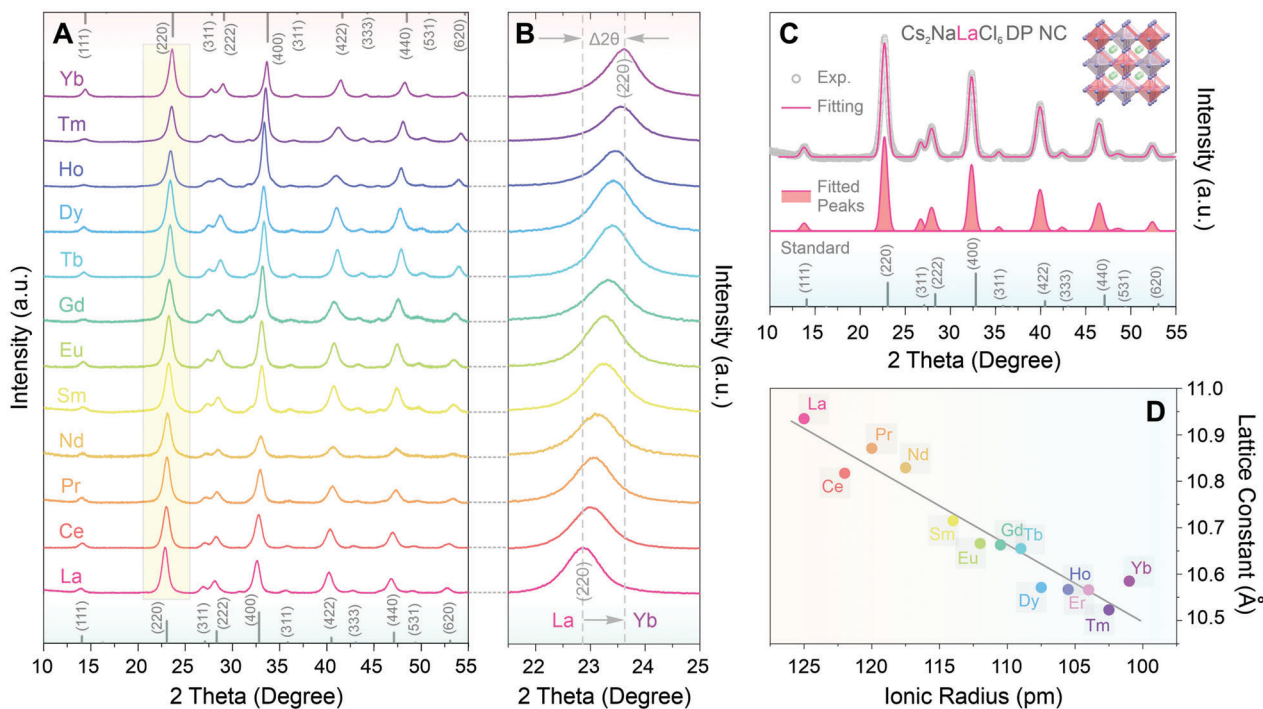
(La to Yb), consistent with a monotonic shrinking trend of the crystal lattice (Figure 1B). The corresponding lattice parameter (*a*) of each Ln-DP NCs can be quantitatively determined through fitting the XRD peaks (Figure 1C; Figures S1-S13 and Table S1, Supporting Information), showing a decrease from 10.935 Å for $Cs_2NaLaCl_6$ NCs to 10.585 Å for $Cs_2NaYbCl_6$ NCs (Figure 1D). The linear relationship between the calculated lattice parameter and the corresponding Ln^{III} cationic radius indicates that the lattice shrinkage is primarily a result of decreasing Ln^{III} size (Figure 1D). Importantly, the synthesized Ln-DP NCs display excellent colloidal stability under N_2 or dry air, whereas negligible changes in the XRD patterns (Figures S14-S18, Supporting Information) were observed for Ln-DP NC samples stored under dry air for at least 4 weeks.

Transmission electron microscopy (TEM) measurements revealed a cuboidal morphology for the synthesized Ln-DP NCs (**Figure 2**A–F, Figure S19, Supporting Information), consistent with the cubic DP crystal phase and an isotropic NC growth fashion.[1d] The average edge lengths of the Ln-DP NCs ranged from 9.2 to 12.2 nm (Figure 2A–F; Figure S19 and Table S2, Supporting Information). High-resolution TEM (HR-TEM) images viewed along the double perovskite [100] direction, and their corresponding fourfold symmetric fast-Fourier transforms further supported the single crystalline nature of $Cs_2NaLnCl_6$ DP NCs (Figure 2A–F). X-ray photoelectron spectroscopy (XPS) measurements established the presence of lanthanide ions in their trivalent oxidation state for each DP NC material (Figure 2G–L Figures S20-S32, Supporting Information). Additional signals for divalent Eu and Yb were observed, which can be attributed to reduction upon exposure to ionizing radiation (Figure 2J,L), enabled by the easily accessible divalent state of europium and ytterbium.[15] XPS survey scans were used to calculate atomic percentages in each material (Table S3, Supporting Information), which were in good agreement with the stoichiometry of the $Cs_2NaLnCl_6$ DPs. Altogether, our experimental results unambiguously establish the successful syntheses of Ln-DP NCs.

2.2. Optical Properties of Ln-DP NCs

Six of the 12 newly synthesized Ln-DP NCs (i.e., $Cs_2NaLnCl_6$ DP NCs, Ln = Ce, Pr, Sm, Eu, Tb, and Yb) showed measurable emission with the PL peaks covering a wide spectral range from UV (Ln = Pr and Ce) through visible (Ln = Tb, Eu, and Sm) to NIR (Ln = Yb and the previously reported Er)[13] (**Figure 3**A). Optical properties were found to be practically unchanged even after 4 weeks of storage in agreement with our observations by XRD (Figures S33-S38, Supporting Information).

$Cs_2NaPrCl_6$ DP NCs displayed the highest energy emission peaks of the $Cs_2NaLnCl_6$ DP NCs, with three major emission peaks observed at 265, 276, and 302 nm (4.68, 4.49, and 4.11 eV, respectively). Each of the emission peaks correspond to Pr-based electronic transitions from the $4f^15d^1$ excited state (term symbol $^3H_4$) to $4f^2$ levels (term symbols ^3H_J, where J = 4–6) (Figure 3A,B).[16] Perovskite-based materials emitting at the UV spectral region have been rarely reported in the literature,[16b,17] and more generally UV-emitting Pr^{3+} materials with reported PLQYs are rare.[16b,c] In the case of $Cs_2NaPrCl_6$ DP NCs, a relatively high PLQY of 14% in the UV-C region was measured, representing

**ADVANCED
SCIENCE NEWS**

www.advancedsciencenews.com

**ADVANCED
OPTICAL
MATERIALS**

www.advopticalmat.de

Figure 1. A) XRD patterns of Cs$_2$NaLnCl$_6$ DP NCs, where Ln = La (bottom) through Ln = Yb (top). Grey bars: reported peak positions of the Cs$_2$NaLaCl$_6$ and Cs$_2$NaYbCl$_6$ DP bulk materials. The XRD trace of previously reported Cs$_2$NaErCl$_6$ DP NCs is included in Figure S11, Supporting Information. B) Zoomed-in XRD pattern for better visualization of the shift of (220) DP diffraction peak. C) XRD pattern of the Cs$_2$NaLaCl$_6$ DP NCs with the fitted cumulative curve (pink line), constituent fitted peaks (pink shades), and standard peak positions (grey bars). D) The linear relationship ($R^2 = 0.92$) between the size of the Ln ion and the experimentally obtained lattice constants of the corresponding DP NCs.
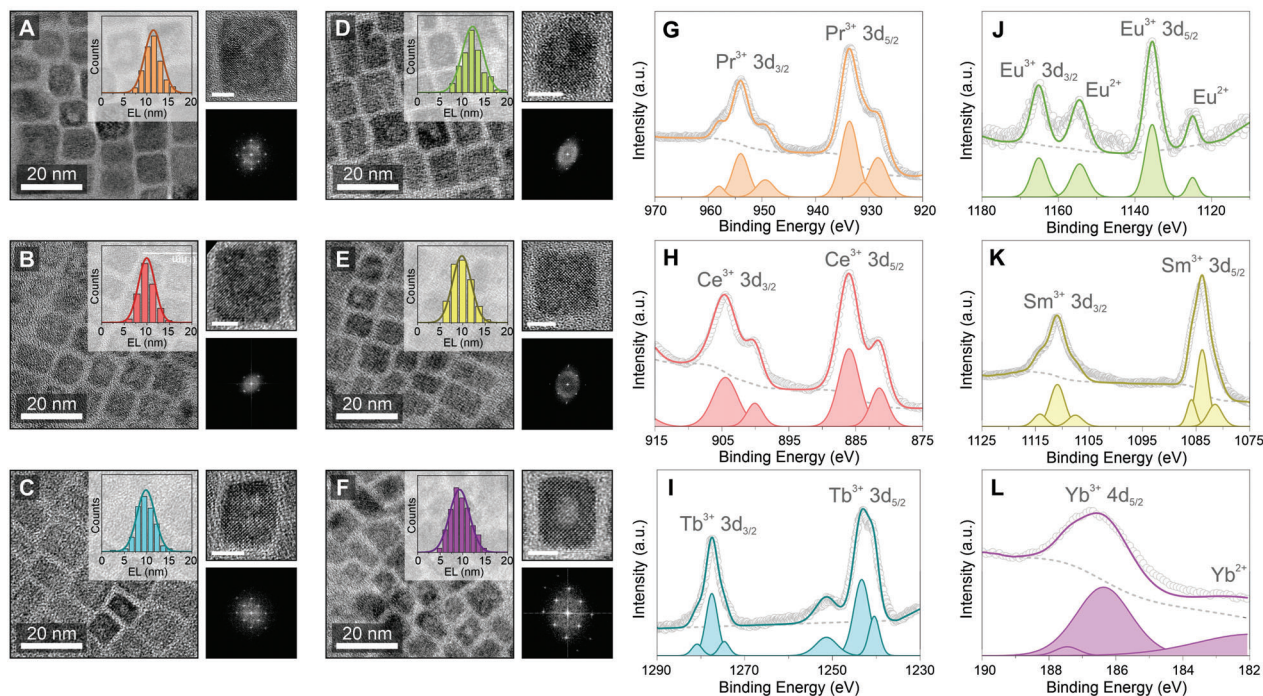
Figure 2. TEM images, size distribution histograms (insets), HR-TEM images (top right), and fast Fourier transform patterns (bottom right) of the six emissive Ln-DP NCs: A) Cs$_2$NaPrCl$_6$, B) Cs$_2$NaCeCl$_6$, C) Cs$_2$NaTbCl$_6$, D) Cs$_2$NaEuCl$_6$, E) Cs$_2$NaSmCl$_6$, and F) Cs$_2$NaYbCl$_6$. HR-TEM scale bars are 5 nm in each case. HR X-ray photoelectron spectroscopy (XPS) spectra of the six samples, confirming the presence of trivalent G) Pr, H) Ce, I) Tb, J) Eu, K) Sm, and L) Yb ions in the corresponding Cs$_2$NaLnCl$_6$ DP NCs. Note: XPS signals from divalent metal ions can be observed in the cases of the Eu- (J) and Yb (L)-based Ln-DP NCs due to X-ray radiation-induced reduction.
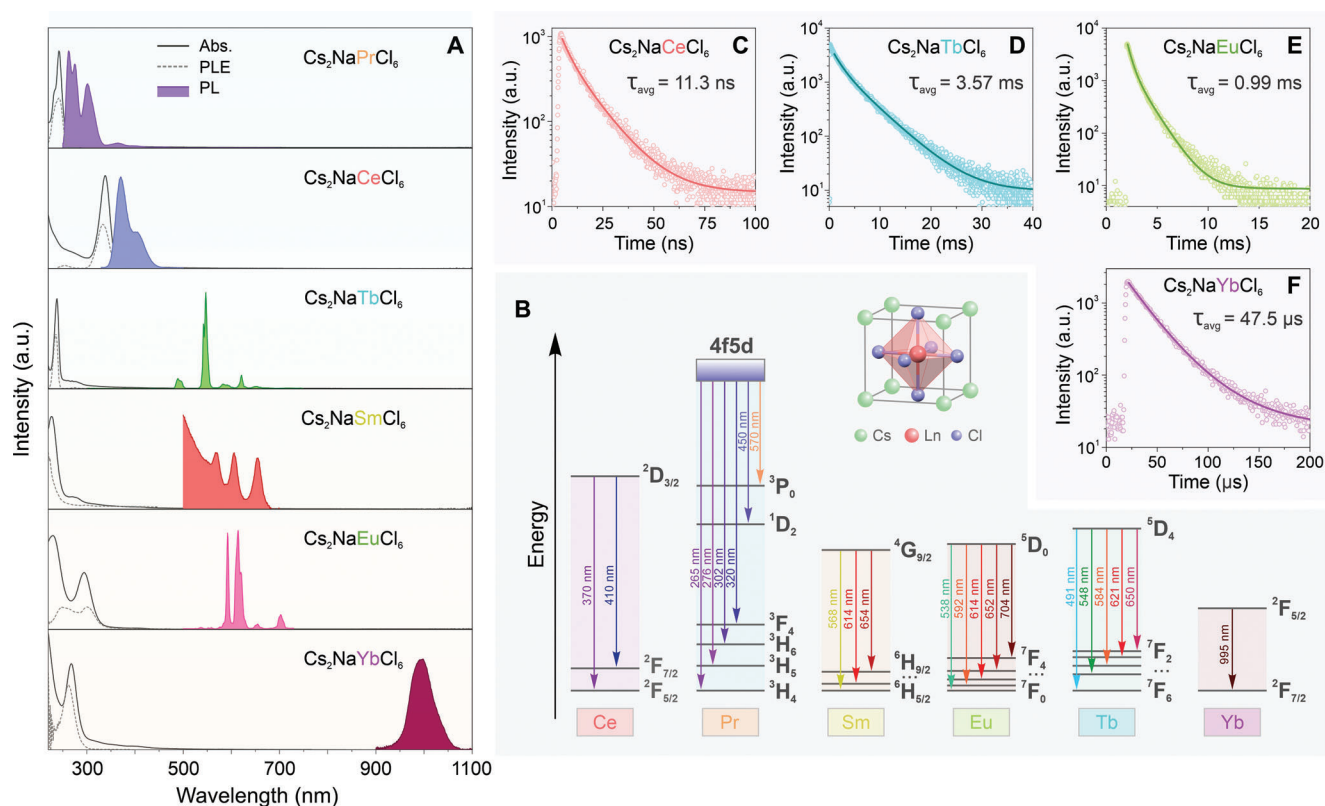
Figure 3. A) Absorption spectra (black solid lines), PLE spectra monitored at the strongest PL peak (grey dashed lines), and PL spectra (colored solid lines with shading) of the six kinds of emissive Ln-DP NCs. B) Energy level diagrams indicating the expected luminescence from the six discussed Ln systems along with their assigned term symbols. Non-emissive levels omitted for clarity.[23] C–F) PL lifetime decay plots (open circles) and fitted curve (solid lines) of the $Cs_2NaCeCl_6$ (C), $Cs_2NaTbCl_6$ (D), $Cs_2NaEuCl_6$ (E), and $Cs_2NaYbCl_6$ (F) DP NCs.

the brightest UV-C emitting perovskite NCs reported to date. A band gap of 4.92 eV was determined by a Tauc plot analysis based on the first narrow (full width at half maximum, FWHM = 330 meV) absorption peak at 245 nm assuming a direct bandgap transition (see discussion below, and Figure S39, Supporting Information). PL excitation (PLE) spectra for all the major emission peaks well overlapped with the absorption profile of the sample, indicating the same energy origin of these emissive pathways (Figures S40-S41). Despite extensive efforts, meaningful lifetime measurements of $Cs_2NaPrCl_6$ NCs were not possible due to the lack of a pulsed excitation source at sufficiently high energies. Access to UV-emitting, all-inorganic perovskites are highly desirable for optoelectronic applications, LED fabrications, and biological disinfecting applications.[17b,18]

$Cs_2NaCeCl_6$ DP NCs displayed UV-A/violet emission with a main peak at 370 nm (3.35 eV) and a shoulder at 410 nm (3.02 eV) (Figure 3A), which can be respectively assigned to the $^2D_{3/2} \rightarrow {}^2F_{5/2}$ and $^2D_{3/2} \rightarrow {}^2F_{7/2}$ electronic transitions within $[CeCl_6]^{3-}$ octahedral units (Figure 3B).[19] A narrow (FWHM = 270 meV) absorption peak centered at around 340 nm serves as the main excitation feature for both emission peaks (Figure S42, Supporting Information), consistent with the observation for the $[CeCl_6]^{3-}$ molecular anion, revealing a high degree of similarity to molecular analogues.[10] A direct bandgap of 3.52 eV was determined for the $Cs_2NaCeCl_6$ DP NCs based on the Tauc plot analysis of the absorption profile (Figure S39, Supporting Informa-

tion). $Cs_2NaCeCl_6$ DP NCs displayed a moderate PLQY of 6% and a PL lifetime of 11.3 ns (Figure 3C and Table S4, Supporting Information). Such a short lifetime decay can be explained by the Laporte-allowed nature of the corresponding Ln 5d→4f transitions (i.e., $^2D_{3/2} \rightarrow {}^2F_{5/2}$ and $^2D_{3/2} \rightarrow {}^2F_{7/2}$), in good agreement with the reported lifetime value for the emission of Ce^{3+} doped $CsPbCl_3$ perovskite NCs.[19]

$Cs_2NaTbCl_6$ DP NCs exhibited a strong green emission originating from the Tb $^5D_4 \rightarrow {}^7F_J$ ($J = 2$–6) transitions, where the most intense peak was located at 550 nm (2.25 eV) (Figure 3A,B).[19] The observed emissive transitions are sensitized by a strong sharp 4f→5d absorption feature at 238 nm (5.21 eV, FWHM = 250 meV) as shown in the PLE spectrum (Figure 3A and Figure S43, Supporting Information), corresponding to a direct bandgap of 5.08 eV (Figure S39, Supporting Information). Importantly, the $Cs_2NaTbCl_6$ DP NCs exhibited the highest PLQY of 45% of all the synthesized Ln-DP NCs in this study, and a long lifetime (3.57 ms) of the $^5D_4$ excited state (Figure 3D; Figure S44 and Table S4, Supporting Information). The PL lifetime was found to be so long due to the spin-forbidden f–f relaxations involved in the emission process (i.e., $^5D_4 \rightarrow {}^7F_J$, $J = 2$–6).[19]

$Cs_2NaSmCl_6$ DP NCs possessed three extremely weak, yet characteristic emission peaks at 569 (2.18 eV), 607 (2.04 eV), and 655 nm (1.89 eV) (Figure 3A), which can be assigned to the Sm $^4G_{9/2} \rightarrow {}^6H_J$ ($J = 5/2$, 7/2, 9/2) electronic transitions.[11e,19] The peaks are sensitized by a single broad (FWHM = 940 meV)

absorption peak at 230 nm as shown in the absorption and PLE spectra (Figure 3A), close to the UV cutoff of 220 nm imposed by double bonds in the oleic acid and oleylamine ligands. This absorption peak was significantly broader (FWHM = 940 meV) than the f–d absorptions seen for the Pr, Ce, and Tb-based DP NCs, and thus it was identified as a ligand to metal charge transfer (LMCT) transition.[10] The PLQY and PL lifetime of the material could not be reliably measured due to the low PL signal intensity.

$Cs_2NaEuCl_6$ DP NCs emitted in the red part of the spectrum, with several narrow emission peaks located between 590–710 nm (Figure 3A) that can be assigned to characteristic Eu[III] electronic transitions associated with $^5D_0 \rightarrow ^7F_J$ ($J = 0$–4) states (Figure 3A,B).[11f,19] The main absorption feature observed at 295 nm was broad (FWHM = 680 meV) and thus it was identified as a LMCT transition with an indirect bandgap of 3.61 eV (Figures S39 and S45, Supporting Information). The PLQY of the sample was determined to be 1.5%, significantly lower than the Pr-, Ce-, and Tb-based DP NCs, likely caused by non-radiative relaxation related to Eu–Eu coupling,[20] as well as the indirect nature of the bandgap (see discussion in the Absorption Features and Their Origins section). A PL lifetime of 0.99 ms was measured for the sample, expectedly long due to the spin-forbidden nature of the f–f relaxation pathways (Figure 3E; Figure S46 and Table S4, Supporting Information).[10] It is worth noting that no divalent europium species were observed in the as-synthesized $Cs_2NaEuCl_6$ DP NCs, evidenced by the lack of characteristic divalent f–d absorption and emission features.

$Cs_2NaYbCl_6$ DP NCs displayed a weak characteristic Yb $^2F_{5/2} \rightarrow ^2F_{7/2}$ emission at 995 nm (1.25 eV) (Figure 3A), in line with the typical Yb-emission feature observed in other Yb-containing perovskite materials.[19] A broad (FWHM = 570 meV) absorption peak at 260 nm was measured and identified as a LMCT transition, leading to an indirect bandgap of 4.12 eV according to the corresponding Tauc plot analysis (Figure S39, Supporting Information).[10] The PL lifetime was measured to be 47.5 µs, which was about tenfold faster than that reported for Yb-doped $CsPbCl_3$ perovskite NCs (Figure 3F and Table S4, Supporting Information).[8d,19] A low PLQY of ≈0.2% along with the fast PL lifetime decay both indicated the presence of significant Yb–Yb coupling induced PL quenching effect.[21] Similar to the $Cs_2NaEuCl_6$ DP NCs, no presence of divalent ytterbium species were detected.

2.3. Absorption Features and Their Origins

Due to the contracted nature of the 4f orbitals, lanthanides in the trivalent oxidation state display characteristic optical transitions that are often minimally perturbed by changes in ligand field.[22] It is well established that emission from Ln[III] materials requires effective sensitization; however, f–f absorption events (Figures S47-S49, Supporting Information)—that are often the lowest energy electronic transitions—are ineffective in this regard due to their Laporte- and spin-forbidden nature (ϵ: 0.1–10 M^{-1} cm^{-1}).[23] Only $Cs_2NaLnCl_6$ DP NCs displaying pronounced absorption features emitted with considerable intensity, therefore identification and assignment of their electronic absorption

features are crucial to understanding and controlling their resulting optical properties. The six emissive Ln-DP NC samples (i.e., the $Cs_2NaLnCl_6$ NCs with Ln = Ce, Pr, Sm, Eu, Tb, and Yb) can be divided into two groups depending on the nature of their absorption features: i) narrow atomic f–d absorption for the Pr-, Ce-, and Tb-based Ln-DP NCs; and ii) broad Cl-to-Ln LMCT absorption for the Eu-, Sm-, and Yb-containing ones.[10] The absorption features observed in Ln-DP NCs are very close in energy to the absorption features of corresponding molecular analogs,[10] and they show minimal quantum confinement effects because of the highly localized valence orbitals (Figure S50, Supporting Information). A similar lack of dimensional confinement was previously described for Bi-based layered DPs.[24]

In the case of f–d absorptions, a 4f-electron is promoted to a high energy unoccupied 5d-orbital, representing a direct transition with negligible spatial charge separation (**Figure 4**A,B). This Laporte- and spin-allowed transition is typically narrower (approximately two to threefold) than charge-transfer transitions (e.g., LMCT),[10] and the energy of the transition blue shifts with increasing Ln[III/IV] reduction potentials.[25] Consistent with these expectations, the first absorption transitions of $Cs_2NaLnCl_6$ DP NCs (Ln = Ce, Pr, and Tb) were relatively narrow (FWHM of about 300 meV in each case), while the energy of the transitions displayed a linear correlation with the corresponding Ln[III/IV] couple ($E_{1/2}$ = +1.7 to +3.2 V vs NHE, Figure 4A).[25] Based on this correlation, the Ln with the next most accessible tetravalent state, Nd[III] ($E_{1/2}$ = +5 V vs NHE), would be predicted to display a 4f-5d absorption feature around ≈170 nm (≈7.3 eV).[25] This transition falls well outside of the measurable spectral region into the deep UV, and was consistent with the effectively featureless absorption and emission profile for $Cs_2NaNdCl_6$ DP NCs (Figure 4A and Figure S33, Supporting Information).

In the case of Cl 3p to Ln 4f LMCT absorption events, an electron is promoted from a filled Cl 3p-orbital to an empty Ln 4f-orbital to generate a transient charge-separated species featuring a divalent Ln[II] ion and a hole on one of the Cl ligands (Figure 4D). Similar divalent Ln species have been identified and detected previously in Ln-doped $CsPbCl_3$ perovskite NCs using transient absorption techniques.[11e] Molecular $[LnCl_6]^{3-}$ (Ln = Sm[III], Eu[III], Tm[III], and Yb[III]) display strong, broad LMCT transitions which red shift with increasing Ln[II/III] reduction potentials. $Cs_2NaLnCl_6$ DP NCs (Ln = Sm, Eu, and Yb) displayed strong, broad LMCT absorption features (FWHM = 570–940 meV), where the energy of the first transition showed a linear correlation with the corresponding Ln[II/III] redox potential (Figure 4C; $E_{1/2}$ = −0.35 to −1.55 V vs NHE).[25] Based on this correlation, the Ln with the next most accessible divalent state, Tm[III] ($E_{1/2}$ = −2.3 V vs NHE),[25] would be predicted to display a LMCT absorption feature around ≈205 nm. The position of this transition would not be directly observable due to spectral overlap with solvent and ligand absorptions, consistent with the effectively featureless absorption and emission profile for $Cs_2NaTmCl_6$ DP NCs (Figure 4C and Figure S33, Supporting Information).

Analogies of the electronic transitions can also be drawn to the extended nanocrystalline solids for their absorptive bandgap transitions. Like direct bandgap transitions, atomic f–d transitions keep the excited electron and the hole localized on the same atom upon excitation, enabling direct radiative recombination
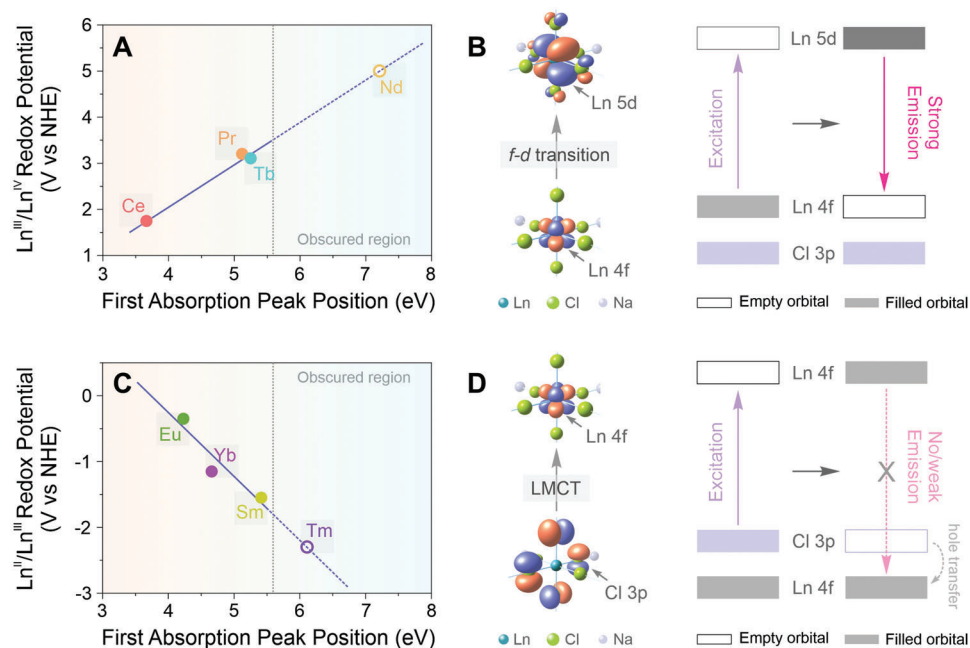
Figure 4. A) For the Ln-DP NCs displaying atomic f–d absorption features, the position of the first absorption peak correlates with the Ln^{III}/Ln^{IV} redox potential. The best fit line was used to estimate the absorption peak position of $Cs_2NaNdCl_6$ DP NCs to be around 7.3 eV. B) Orbital diagrams illustrating a typical atomic f–d transition event (left), and a schematic illustrating excitation and emission resembling direct bandgap transitions (right). C) For Ln-DP NCs showing LMCT features, the position of the first absorption peak correlates with the Ln^{II}/Ln^{III} redox potential. The fitting line was used to estimate the absorption peak position of $Cs_2NaTmCl_6$ DP NCs to be around 6.1 eV. D) Orbital diagrams illustrating a typical LMCT event (left), and a schematic illustrating excitation and emission resembling indirect bandgap transitions (right). Note: a hole transfer process is required for radiative f–f relaxation in this case.

without spatial separation (Figure 4B). In contrast, LMCT transitions lead to the transfer of the excited electron from the ligand to the metal center, resulting in a spatial separation of the electron and the hole in the excited state as seen for indirect bandgap transitions. Charge-separated excited states involved in this LMCT process can only be emissive following a hole transfer step from Cl 3p- to Ln 4f-orbitals (Figure 4D).[11d,e] However, due to the slow hole transfer process (few ns, multiple orders of magnitude slower than the electron transfer process depending on the energy difference),[11d,e,26] the energy of charge separated excited states is more likely dissipated through nonradiative pathways such as phonon-assisted energy transfer, or transferred to dark sites prior to luminescence.[27] Consequently, the PLQYs for the materials with atomic f–d transitions are expected to be higher than those with LMCT transitions. A trend consistent with these explanations was observed for $Cs_2NaLnCl_6$ DP NCs; DP NCs with direct bandgap absorptions (i.e., 4f-5d transitions; Ce, Pr, Tb) displayed dramatically higher PLQYs than those with indirect bandgap absorptions (i.e., LMCT transitions; Sm, Eu, and Yb) (Figure 4). These findings were also consistent with the observed photophysical behavior of $Cs_2NaErCl_6$ DP NCs and their Sb^{III}- and Bi^{III}-doped derivatives. The UV–vis spectrum of $Cs_2NaErCl_6$ DP NC lack strong absorption features capable of sensitization, which leads to low PLQY. Sb^{III}- and Bi^{III}-doping introduces strong, Laporte- and spin-allowed Sb and Bi-based absorption transitions, which increased the PL intensity dramatically.[13]

2.4. Computational Analysis

To gain a deeper understanding of the electronic structures of $Cs_2NaLnCl_6$ DPs, DFT[28] calculations were employed. Band structures and density of states (DOS) DFT calculations for the six emissive materials (i.e., $Cs_2NaLnCl_6$ with Ln = Ce, Pr, Sm, Eu, Tb, and Yb) were carried out using the common plane wave approach,[29] employing the Perdew–Burke–Ernzerhof (PBE, generalized gradient approximation)[30] functional with non-linear core corrections and scalar relativistic effects (see Supporting Information for calculation details). Calculated lattice constants of the six selected $Cs_2NaLnCl_6$ were in good agreement with reported values, with computed values being systematically overestimated by ≈0.2 Å (Table S5, Supporting Information).[12b,31] Across all these six systems, the valence band maximum was dominated by Cl 3p character with varying contributions from Ln 4f-orbitals, while the conduction band minimum is primarily composed of Ln 4f and 5d orbitals (**Figure 5**), in agreement with experimental findings using Ln-DP bulk solids,[32] albeit with significant differences in the relative energies of the spin polarized 4f states.

Calculations for the Ce, Pr, and Tb $Cs_2NaLnCl_6$ DP NCs successfully predicted energetically accessible, direct bandgap transitions corresponding to Laporte- and spin-allowed Ln-centered 4f→5d transitions at 2.29, 2.77, and 3.83 eV (Figure 5A,B,E). While the calculated transition energies were systematically underestimated by ≈1.2 eV from the experimentally determined
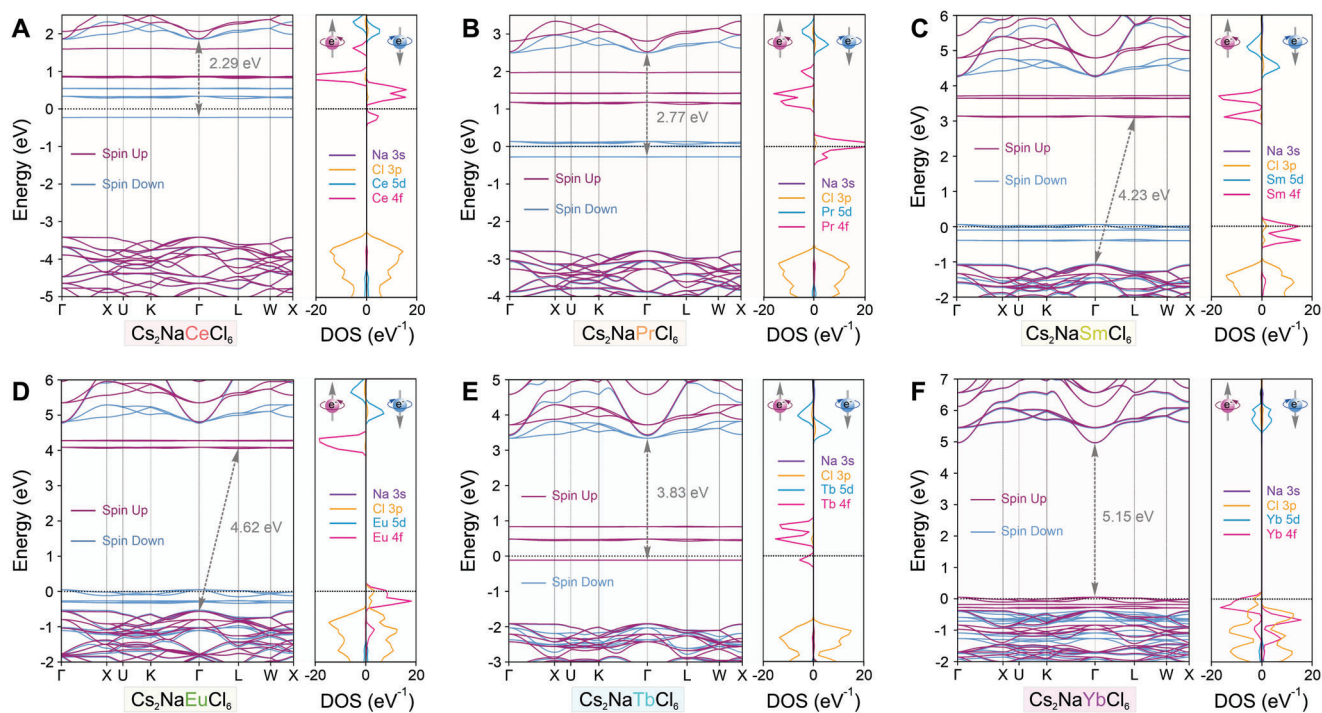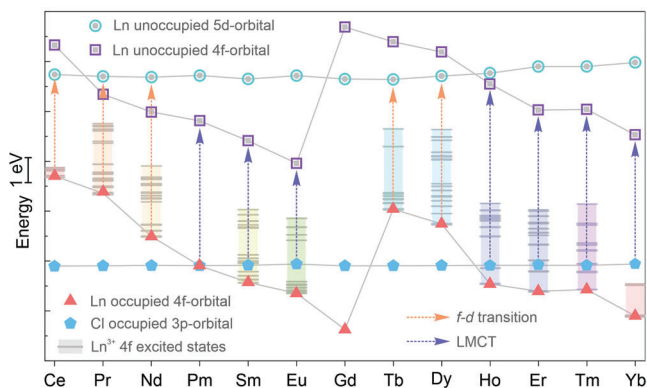
Figure 5. The calculated band structures (left) and the corresponding DOSs (right) of the six emissive Ln-DP systems: A) $Cs_2NaCeCl_6$, B) $Cs_2NaPrCl_6$, C) $Cs_2NaSmCl_6$, D) $Cs_2NaEuCl_6$, E) $Cs_2NaTbCl_6$, and F) $Cs_2NaYbCl_6$. Spin down (blue solid lines) and spin up (purple solid lines) are differentiated in each case. The observed band gap transitions are marked with dashed arrows. Valence band maxima are set to 0 eV.

direct bandgaps (3.52, 4.92, and 5.08 eV), the trend in their relative energies was successfully reproduced within the series (Figure S39, Supporting Information). Calculations of Sm and Eu $Cs_2NaLnCl_6$ DP NCs (Figure 5C,D) also successfully predicted energetically accessible, indirect bandgap transitions corresponding to LMCT Cl 3p→Ln 4f transitions (Sm_{calc}: 4.23 eV, Sm_{expt}: 4.71 eV; Eu_{calc}: 4.62 eV, Eu_{expt}: 3.61 eV). In contrast, calculations of $Cs_2NaYbCl_6$ DP NCs predicted a direct bandgap transition corresponding to a high-energy (5.15 eV), parity-allowed Ln 4f→5d transition, instead of an indirect bandgap transition originating from a LMCT Cl 3p→Ln 4f transition observed in our experiments and prior literature reports (Figure 5F).

While our plane-wave calculations reproduced some general properties of $Cs_2NaLnCl_6$ DP NCs, they incorrectly predicted the nature of the bandgap for Yb and featured relatively large energy differences for calculated and experimental bandgap transitions within the series. Due to the highly correlated nature of 4f states, the band structures of Ln-containing materials can be non-trivial to reproduce by single determinant methods.[33] While multi-configurational approaches, such as complete active space self-consistent field, can be used to model multi-reference character, these methods scale poorly with active space size and can be cost-prohibitive for large active spaces.[34] Given these restrictions, and the striking similarities in the optical properties of $Cs_2NaLnCl_6$ DPs NCs and $[LnCl_6]^{3-}$ molecular analogs, we also interrogated the electronic structure of previously studied small molecule models, $[Na_6LnCl_6]^{3+}$ (Ln = Ce–Yb), by DFT.[35] All calculations were carried out using the hybrid PBE functional and property-optimized def2-tzvpp(d) basis sets for

Ln reported by Rappoport.[36] Geometry-optimized structures of $[Na_6LnCl_6]^{3+}$ were in good agreement with the crystal structures of $Cs_2NaLnCl_6$, where calculated and experimentally determined Ln–Cl bond distances were within 0.04 Å of one another (Table S6, Supporting Information). Energies of the highest occupied Cl 3p and Ln 4f orbitals as well as the lowest unoccupied Ln 4f and 5d orbitals (Ln = Ce–Yb) were calculated in the ground state, but this simple model was also insufficient to correctly predict the nature of observed absorption features (Figure S51, Supporting Information). However, time-dependent DFT (TD-DFT) calculations carried out on the optimized structures of $[Na_6LnCl_6]^{3+}$ at the same level of theory effectively captured the main sensitization transitions for $Cs_2NaLnCl_6$ DPs NCs. Ce^{III}, Pr^{III}, and Tb^{III} clearly featured 4f→5d transitions at 4.16, 5.16, and 2.47 eV, respectively, while Sm^{III}, Eu^{III}, and Yb^{III} featured Cl 3p to Ln 4f LMCT transitions at 2.48, 1.59, and 2.66 eV, respectively (Table S7, Supporting Information). Even with the observed discrepancies in transition energies, TD-DFT was able to correctly predict the lowest energy allowed electronic transitions of all six Ln-DP NCs showing features in the UV–vis spectrum. The calculated transition energies differed significantly from experimentally obtained results, highlighting the challenges and limitations in the calculation of lanthanide 4f electronic states.

With both experimental and computational data in hand, we set out to construct a semi-empirical energy diagram capable of summarizing the electronic structure and optical properties of $Cs_2NaLnCl_6$ DP NCs. In order to construct a diagram with relative orbital energies of sufficient accuracy, the highest occupied and unoccupied 4f orbital energies were corrected by

**ADVANCED
SCIENCE NEWS**

www.advancedsciencenews.com

**ADVANCED
OPTICAL
MATERIALS**

www.advopticalmat.de

Figure 6. Relative energy diagram of the highest occupied Cl 3p orbitals (blue pentagons), highest occupied Ln 4f orbitals (red triangles), lowest unoccupied Ln 4f orbitals (purple open squares), and lowest unoccupied Ln 5d orbitals (cyan open circles) across the Ln series. Horizontal grey lines indicate positions of Ln^{III} $4f^n$ excited states in $Cs_2NaLnCl_6$ bulk materials with the consideration of spin-orbit coupling. Note: high-energy calculated Ln^{III} $4f^n$ excited states are not included. Excited states of radioactive Pm are not included due to the lack of experimental data in DP systems. The expected lowest energy absorptions are indicated by pink arrows (f–d transitions) or blue arrows (LMCTs).

using experimentally determined values for the lowest energy 4f→5d or LMCT transitions, where Cl 3p and Ln 5d orbital energies were taken from DFT calculations of the molecular analogs, $[Na_3LnCl_6]^{3+}$. LMCT transitions were used to adjust the DFT-calculated energies of unoccupied 4f orbitals relative to Cl 3p orbitals, while 4f→5d transitions were used to correct occupied 4f orbital energies with respect to Ln 5d orbitals (see Supporting Information for correction details). Select sections of the excited Ln^{III} 4f manifold were constructed using previously reported, 4f orbital energies experimentally determined for bulk $Cs_2NaLnCl_6$ (**Figure 6**).[37] Based on the diagram, the lowest energy absorptions for the Ln with filled 4f-orbital energies above that of the Cl 3p-orbitals (the cases of Ce, Pr, Nd, Tb, and Dy) were predicted to be dominated by the f→d atomic transitions (Figure 6, red dashed line arrows). The f→d transition energies increased with rising $Ln^{III/IV}$ redox potential (Ce < Pr ≈ Tb < Dy) as expected and discussed above (Figures 4 and 5).[10] In contrast, the first absorption feature of Ln with filled 4f-orbitals below the Cl 3p-orbital energy levels should be dominated by LMCT transitions, as for the cases of Sm, Eu, Gd, Ho, Er, Tm, and Yb (Figure 6). The corresponding LMCT transition energies (Figure 6, blue dashed line arrows) agreed reasonably well with the $Ln^{II/III}$ redox potential (Eu < Yb ≈ Sm < Tm).[10] A summary of predicted and measured electronic transition energies and bandgaps can be found in Table S8, Supporting Information. The suitability of this semi-empirical model was further validated by comparing the relative orbital energies with experimentally determined values from valence band XPS spectra for the selected $Cs_2NaLnCl_6$ (Ln = Ce, Pr, Tb, and Gd; Figures S52-S55, Supporting Information). Energy differences between the filled Cl $3p_{3/2}$ and Ln 4f orbitals measured by XPS were in good agreement with the corrected values constructed in the semi-empirical model, and provided further support for our model (Figure S56, Supporting Information).

2.5. Alloyed Ln-DP NCs with Enhanced Optical Properties

Alloying and doping have been used extensively in the past to enhance optical properties of NCs, as alloyed nanomaterials can deliver properties inaccessible to physical mixtures of different components.[3t,8f,9a,19] The successful synthesis of alloyed perovskite materials can be challenging, as stable combinations require appropriate matching of the introduced cation's size with the host material's tolerance factor while keeping charge balance in mind.[38] Given the similar ionic radii of Ln^{III} ions,[39] a large range of alloyed DP NCs should be accessible. To demonstrate this possibility, two representative examples of alloyed $Cs_2NaLnCl_6$ DP NCs were synthesized.
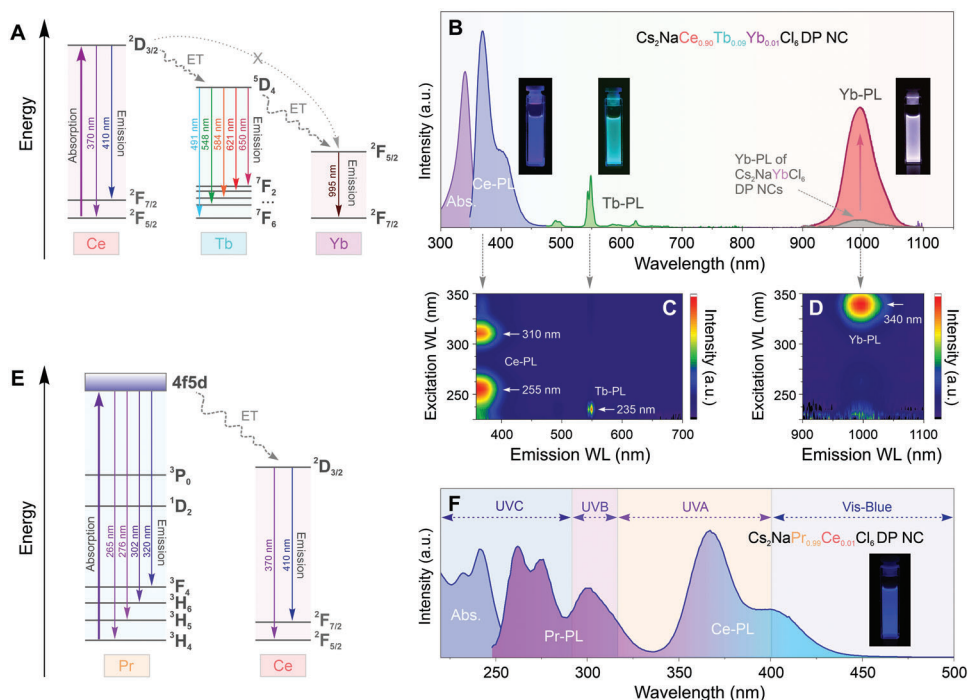
2.5.1. $Cs_2NaCe_{0.90}Tb_{0.09}Yb_{0.01}Cl_6$ DP NCs

Ternary alloys showing emission across the UV, visible, and NIR range are interesting synthetic targets for light emission purposes, for multiplex imaging in biological setups, or for the synthesis of advanced anti-counterfeit materials.[3t,9a,11c,40] Using the hot injection methodology described for Ln-pure DP NCs (see detailed synthetic procedure in Supporting Information), $Cs_2NaCe_{0.90}Tb_{0.09}Yb_{0.01}Cl_6$ alloyed Ln-DP NCs were successfully synthesized (Figures S57, S59, and S60, Supporting Information). Under 340 nm excitation, the $Cs_2NaCe_{0.90}Tb_{0.09}Yb_{0.01}Cl_6$ DP NCs displayed PL peaks from all three Ln components: Ce^{III} emission at 365 nm, Tb^{III} emission at 550 nm, and Yb^{III} emission at 995 nm (**Figure 7**A,B). Importantly, the NIR Yb-PL peak at 995 nm was significantly increased in intensity as compared to the pure $Cs_2NaYbCl_6$ DP NCs (Figure 7B). The PLQY in the NIR range (i.e., Yb-PL) was determined to be 6%, indicating a ≈30-fold enhancement as compared to that of the pure $Cs_2NaYbCl_6$ DP NCs (Figure 7B). This enhancement effect was significantly diminished if the Tb "bridge" was omitted, evidenced by a much lower NIR PLQY of ≈1% for the $Cs_2NaCe_{0.99}Yb_{0.01}Cl_6$ DP NCs synthesized analogously (Figure S63, Supporting Information). Furthermore, the alloyed $Cs_2NaCe_{0.90}Tb_{0.09}Yb_{0.01}Cl_6$ Ln-DP NCs also showed an excitation-dependent luminescence property. The peak intensities of both visible (Figure 7C) and NIR (Figure 7D) emissions changed dramatically depending on the excitation wavelength, which cannot be seen when individual Ln-pure $Cs_2NaLnCl_6$ (Ln = Ce, Tb, and Yb) NCs are mixed with the appropriate ratio (Figure S64, Supporting Information). The Ce-PL can be sensitized by the excitation light with two wavelengths in comparable intensities: 255 and 310 nm. While the strongest Tb-PL can only be observed under 235 nm excitation, the strongest Yb-PL is displayed only when exciting at 340 nm (Figure 7D).

2.5.2. $Cs_2NaPr_{0.99}Ce_{0.01}Cl_6$ DP NCs

UV-emissive perovskite nanomaterials are exceedingly rare and highly sought after, and such materials hold the potential to be utilized in biomedical settings as disinfecting light sources,[41] or in fabrications of high-energy LEDs as the UV-emissive component.[42] Given our discovery of $Cs_2NaCeCl_6$ and $Cs_2NaPrCl_6$ DP NCs capable of emitting in the UV-C and UV-A region, we synthesized $Cs_2NaPr_{0.99}Ce_{0.01}Cl_6$ DP NCs using an

Figure 7. A) Energy level diagram illustrating the energy transfer from the Ce host to the Yb dopant bridged by the Tb component for $Cs_2NaCe_{0.90}Tb_{0.09}Yb_{0.01}Cl_6$ alloyed Ln-DP NCs. B) Absorption and PL spectra of the $Cs_2NaCe_{0.90}Tb_{0.09}Yb_{0.01}Cl_6$ alloyed Ln-DP NCs display emission from all three components under 340 nm excitation. C,D) 2D contour maps at visible (C) and NIR (D) regions for the $Cs_2NaCe_{0.90}Tb_{0.09}Yb_{0.01}Cl_6$ DP NCs, showing an excitation-dependent PL feature of the sample. E) Energy level diagram illustrating the energy transfer occurs from the Pr host to the Ce component of the $Cs_2NaCe_{0.99}Ce_{0.01}Cl_6$ alloyed Ln-DP NCs. F) Absorption and PL spectra of the $Cs_2NaCe_{0.99}Ce_{0.01}Cl_6$ DP NCs, displaying broadband UV-C to visible-blue emission.

appropriate mixture of $Ce(OAc)_3$ and $Pr(OAc)_3$ precursors (see details in Supporting Information; Figures S58, S59, S61, and S62, Supporting Information). The obtained $Cs_2NaPr_{0.99}Ce_{0.01}Cl_6$ DP NCs emit across the UV-C to UV-A, and into the visible blue spectral range, representing the first example of a broad UV-emitting perovskite nanomaterial (Figure 7E,F).

3. Conclusion

In summary, we demonstrate the colloidal synthesis of $Cs_2NaLnCl_6$ (Ln = La–Nd, Sm–Yb) Ln-DP NCs using a hot injection approach. The obtained Ln-DP NCs display emissions covering a wide wavelength range from deep UV to NIR. The $Cs_2NaPrCl_6$ and $Cs_2NaCeCl_6$ DP NCs display strong UV emission, with the $Cs_2NaPrCl_6$ DP NCs being the only UV-C emitting halide perovskite nanomaterial known to date. Using the combination of molecular analogs and DFT calculations, a comprehensive understanding of energy levels and electronic transitions in the $Cs_2NaLnCl_6$ DP systems was achieved. Due to the similar ionic sizes and high miscibility of Ln elements, we have successfully synthesized alloyed Ln-DP NCs simultaneously containing multiple Ln components, which show unique optical properties that are inaccessible by their pure-Ln counterparts. Our study not only provides important fundamental understandings on the Ln-DP materials, but also offers a family of new DP nanomaterials promising for a spectrum of applications ranging

from high-energy LEDs and secure anti-counterfeiting paints to biomedical disinfections.

Supporting Information

Supporting Information is available from the Wiley Online Library or from the author.

Conflict of Interest

The authors declare no conflict of interest.

Data Availability Statement

The data that support the findings of this study are available from the corresponding author upon reasonable request.

[1] a) A. K. Jena, A. Kulkarni, T. Miyasaka, *Chem. Rev.* **2019**, *119*, 3036; b) H. Utzat, W. Sun, A. E. K. Kaplan, F. Krieg, M. Ginterseder, B. Spokoyny, N. D. Klein, K. E. Shulenberger, C. F. Perkinson, M. V. Kovalenko, M. G. Bawendi, *Science* **2019**, *363*, 1068; c) M. V. Kovalenko, L. Protesescu, M. I. Bodnarchuk, *Science* **2017**, *358*, 745; d) L. Protesescu, S. Yakunin, M. I. Bodnarchuk, F. Krieg, R. Caputo, C. H. Hendon, R. X. Yang, A. Walsh, M. V. Kovalenko, *Nano Lett.* **2015**, *15*, 3692; e) H. Yang, Y. Zhang, K. Hills-Kimball, Y. Zhou, O. Chen, *Sustainable Energy Fuels* **2018**, *2*, 2381; f) K. Hills-Kimball, H. Yang, T. Cai, J. Wang, O. Chen, *Adv. Sci.* **2021**, *8*, 2100214.

[2] a) J. Li, H. L. Cao, W. B. Jiao, Q. Wang, M. Wei, I. Cantone, J. Lü, A. Abate, *Nat. Commun.* **2020**, *11*, 310; b) P. Su, Y. Liu, J. Zhang, C. Chen, B. Yang, C. Zhang, X. Zhao, *J. Phys. Chem. Lett.* **2020**, *11*, 2812.

[3] a) I. Infante, L. Manna, *Nano Lett.* **2021**, *21*, 6; b) J. Zhou, J. Luo, X. Rong, P. Wei, M. S. Molokeev, Y. Huang, J. Zhao, Q. Liu, X. Zhang, J. Tang, Z. Xia, *Adv. Opt. Mater.* **2019**, *7*, 1900139; c) Y. Liu, A. Nag, L. Manna, Z. Xia, *Angew. Chem., Int. Ed.* **2021**, *60*, 11592; d) F. Igbari, R. Wang, Z. K. Wang, X. J. Ma, Q. Wang, K. L. Wang, Y. Zhang, L. S. Liao, Y. Yang, *Nano Lett.* **2019**, *19*, 2066; e) S. E. Creutz, E. N. Crites, M. C. De Siena, D. R. Gamelin, *Nano Lett.* **2018**, *18*, 1118; f) F. Locardi, M. Cirignano, D. Baranov, Z. Dang, M. Prato, F. Drago, M. Ferretti, V. Pinchetti, M. Fanciulli, S. Brovelli, L. De Trizio, L. Manna, *J. Am. Chem. Soc.* **2018**, *140*, 12989; g) A. B. Wong, Y. Bekenstein, J. Kang, C. S. Kley, D. Kim, N. A. Gibson, D. Zhang, Y. Yu, S. R. Leone, L. W. Wang, A. P. Alivisatos, P. Yang, *Nano Lett.* **2018**, *18*, 2060; h) J. Huang, T. Lei, M. Siron, Y. Zhang, S. Yu, F. Seeler, A. Dehestani, L. N. Quan, K. Schierle-Arndt, P. Yang, *Nano Lett.* **2020**, *20*, 3734; i) B. Yang, J. Chen, F. Hong, X. Mao, K. Zheng, S. Yang, Y. Li, T. Pullerits, W. Deng, K. Han, *Angew. Chem., Int. Ed.* **2017**, *56*, 12471; j) B. Yang, J. Chen, S. Yang, F. Hong, L. Sun, P. Han, T. Pullerits, W. Deng, K. Han, *Angew. Chem., Int. Ed.* **2018**, *57*, 5359; k) H. Yang, T. Cai, L. Dube, O. Chen, *Chem. Sci.* **2022**, *13*, 4874; l) T. Cai, W. Shi, S. Hwang, K. Kobbekaduwa, Y. Nagaoka, H. Yang, K. Hills-Kimball, H. Zhu, J. Wang, Z. Wang, Y. Liu, D. Su, J. Gao, O. Chen, *J. Am. Chem. Soc.* **2020**, *142*, 11927; m) H. Yang, T. Cai, E. Liu, K. Hills-Kimball, J. Gao, O. Chen, *Nano Res.* **2019**, *13*, 282; n) T. Cai, L. Dube, P. Saghy, H. Yang, O. Chen, *Trends Chem.* **2022**, *5*, 29; o) L. N. Quan, M. Yuan, R. Comin, O. Voznyy, E. M. Beauregard, S. Hoogland, A. Buin, A. R. Kirmani, K. Zhao, A. Amassian, D. H. Kim, E. H. Sargent, *J. Am. Chem. Soc.* **2016**, *138*, 2649; p) A. Bibi, I. Lee, Y. Nah, O. Allam, H. Kim, L. N. Quan, J. Tang, A. Walsh, S. S. Jang, E. H. Sargent, D. H. Kim, *Mater. Today* **2021**, *49*, 123; q) J. Luo, X. Wang, S. Li, J. Liu, Y. Guo, G. Niu, L. Yao, Y. Fu, L. Gao, Q. Dong, C. Zhao, M. Leng, F. Ma, W. Liang, L. Wang, S. Jin, J. Han, L. Zhang, J. Etheridge, J. Wang, Y. Yan, E. H. Sargent, J. Tang, *Nature* **2018**, *563*, 541; r) B. Vargas, G. Rodríguez-López, D. Solis-Ibarra, *ACS Energy Lett.* **2020**, *5*, 3591; s) B. Vargas, E. Ramos, E. Pérez-Gutiérrez, J. C. Alonso, D. Solis-Ibarra, *J. Am. Chem. Soc.* **2017**, *139*, 9116; t) J. Li, J. Xiao, T. Lin, Z. Yan, X. Han, *J. Mater. Chem. C* **2022**, *10*, 7626; u) Y. Bekenstein, J. C. Dahl, J. Huang, W. T. Osowiecki, J. K. Swabeck, E. M. Chan, P. Yang, A. P. Alivisatos, *Nano Lett.* **2018**, *18*, 3502; v) B. Yang, X. Mao, F. Hong, W. Meng, Y. Tang, X. Xia, S. Yang, W. Deng, K. Han, *J. Am. Chem. Soc.* **2018**, *140*, 17001.

[4] a) H. Tang, Y. Xu, X. Hu, Q. Hu, T. Chen, W. Jiang, L. Wang, W. Jiang, *Adv. Sci.* **2021**, *8*, 2004118; b) W. Lee, S. Hong, S. Kim, *J. Phys. Chem. C* **2019**, *123*, 2665.

[5] L. Chu, W. Ahmad, W. Liu, J. Yang, R. Zhang, Y. Sun, J. Yang, X. Li, *Nano-Micro Lett.* **2019**, *11*, 16.

[6] C. E. Lambert, M. L. Ledrich, in *Encyclopedia of Toxicology*, 3rd ed., Academic Press, San Diego, CA **2014**, pp. 43–47.

[7] S. Cotton, *Lanthanide and Actinide Chemistry*, 2nd ed., Wiley, New York **2006**.

[8] a) S. L. Zuo, P. Chen, C. F. Pan, *Rare Met.* **2020**, *39*, 1113; b) G. Rooh, H. Kang, H. J. Kim, H. Park, S. Kim, *J. Cryst. Growth* **2009**, *311*, 2470; c) Y. Chen, R. Zeng, Q. Wei, S. Zhang, B. Luo, C. Chen, X. Zhu, S. Cao, B. Zou, J. Z. Zhang, *J. Phys. Chem. Lett.* **2022**, *13*, 8529; d) T. Cai, J. Wang, W. Li, K. Hills-Kimball, H. Yang, Y. Nagaoka, Y. Yuan, R. Zia, O. Chen, *Adv. Sci.* **2020**, *7*, 2001317; e) Y. Zhou, J. Chen, O. M. Bakr, O. F. Mohammed, *ACS Energy Lett.* **2021**, *6*, 739; f) S. Wen, J. Zhou, K. Zheng, A. Bednarkiewicz, X. Liu, D. Jin, *Nat. Commun.* **2018**, *9*, 2415; g) A. Gaita-Ariño, H. Prima-García, S. Cardona-Serra, L. Escalera-Moreno, L. E. Rosaleny, J. J. Baldoví, *Inorg. Chem. Front.* **2016**, *3*, 568.

[9] a) S. Jin, R. Li, H. Huang, N. Jiang, J. Lin, S. Wang, Y. Zheng, X. Chen, D. Chen, *Light: Sci. Appl.* **2022**, *11*, 52; b) J. C. G. Bünzli, *Trends Chem.* **2019**, *1*, 751; c) R. D. L. Gaspar, P. R. Fortes, I. O. Mazali, F. A. Sigoli, I. M. Raimundo, *ChemistrySelect* **2018**, *3*, 10491; d) J. J. Baldoví, L. E. Rosaleny, V. Ramachandran, J. Christian, N. S. Dalal, J. M. Clemente-Juan, P. Yang, U. Kortz, A. Gaita-Ariño, E. Coronado, *Inorg. Chem. Front.* **2015**, *2*, 893.

[10] J. L. Ryan, K. C. Jorgensen, *J. Phys. Chem.* **1966**, *70*, 2845.

[11] a) H. Arfin, J. Kaur, T. Sheikh, S. Chakraborty, A. Nag, *Angew. Chem., Int. Ed.* **2020**, *59*, 11307; b) J. Nie, H. Li, S. Fang, B. Zhou, Z. Liu, F. Chen, Y. Wang, Y. Shi, *Cell Rep. Phys. Sci.* **2022**, *3*, 100820; c) Z. Zeng, B. Huang, X. Wang, L. Lu, Q. Lu, M. Sun, T. Wu, T. Ma, J. Xu, S. Wang, Y. Du, C. H. Yan, *Adv. Mater.* **2020**, *32*, 2004506; d) M. Zeng, F. Artizzu, J. Liu, S. Singh, F. Locardi, D. Mara, Z. Hens, R. Van Deun, *ACS Appl. Nano Mater.* **2020**, *3*, 4699; e) W. J. Chang, S. Irgen-Gioro, S. Padgaonkar, R. López-Arteaga, E. A. Weiss, *J. Phys. Chem. C* **2021**, *125*, 25634; f) L. Zhang, M. Yuan, *Light: Sci. Appl.* **2022**, *11*, 99.

[12] a) T. R. Faulkner, J. P. Morley, F. S. Richardson, R. W. Schwartz, *Mol. Phys.* **1980**, *40*, 1481; b) L. R. Morss, M. Siegal, L. Stenger, N. Edelstein, *Inorg. Chem.* **1970**, *9*, 1771.

[13] R. Wu, P. Han, D. Zheng, J. Zhang, S. Yang, Y. Zhao, X. Miao, K. Han, *Laser Photonics Rev.* **2021**, *15*, 2100218.

[14] a) V. K. Lamer, R. H. Dinegar, *J. Am. Chem. Soc.* **1950**, *72*, 4847; b) C. B. Murray, C. R. Kagan, M. G. Bawendi, *Annu. Rev. Mater. Sci.* **2000**, *30*, 545.

[15] a) Y. Kohara, G. Okada, I. Tsuyumoto, E. Kusano, H. Nanto, *Mater. Lett.* **2021**, *303*, 130502; b) R. Nagaishi, T. Kimura, Y. Yoshida, T. Kozawa, S. Tagawa, *J. Phys. Chem. A* **2002**, *106*, 9036; c) H. Nalumaga, J. J. Schuyt, R. D. Breukers, G. V. M. Williams, *Mater. Res. Bull.* **2022**, *145*, 111562; d) D. S. McClure, Z. Kiss, *J. Chem. Phys.* **2004**, *39*, 3251.

[16] a) M. Runowski, P. Woźny, I. R. Martín, V. Lavín, S. Lis, *J. Lumin.* **2019**, *214*, 116571; b) X. Wang, Y. Mao, *J. Mater. Chem. C* **2022**, *10*, 3626; c) X. Wang, Y. Chen, F. Liu, Z. Pan, *Nat. Commun.* **2020**, *11*, 2040.

[17] a) S. C. Lim, H. P. Lin, W. L. Tsai, H. W. Lin, Y. T. Hsu, H. Y. Tuan, *Nanoscale* **2017**, *9*, 3747; b) Y. Zhang, X. Cheng, D. Tu, Z. Gong, R. Li, Y. Yang, W. Zheng, J. Xu, S. Deng, X. Chen, *Angew. Chem., Int. Ed.* **2021**, *60*, 9693.

[18] a) M. Biasin, A. Bianco, G. Pareschi, A. Cavalleri, C. Cavatorta, C. Fenizia, P. Galli, L. Lessio, M. Lualdi, E. Tombetti, A. Ambrosi, E. M. A. Redaelli, I. Saulle, D. Trabattoni, A. Zanutta, M. Clerici, *Sci. Rep.* **2021**, *11*, 6260; b) M. Shimizu, T. Sakurai, *Aggregate* **2022**, *3*, e144.

[19] G. Pan, X. Bai, D. Yang, X. Chen, P. Jing, S. Qu, L. Zhang, D. Zhou, J. Zhu, W. Xu, B. Dong, H. Song, *Nano Lett.* **2017**, *17*, 8005.

[20] P. A. Hansen, C. S. Granerød, Ø. Prytz, O. Nilsen, *J. Lumin.* **2019**, *215*, 116618.

[21] Z. Wang, A. Meijerink, *J. Phys. Chem. C* **2018**, *122*, 26298.

[22] J. C. G. Bünzli, C. Piguet, *Chem. Soc. Rev.* **2005**, *34*, 1048.

[23] B. G. Wybourne, L. Smentek, *Optical Spectroscopy of Lanthanides: Magnetic and Hyperfine Interactions*, Taylor and Francis, London **2007**.

[24] M. Pantaler, V. Diez-Cabanes, V. I. E. Queloz, A. Sutanto, P. A. Schouwink, M. Pastore, I. García-Benito, M. K. Nazeeruddin, D. Beljonne, D. C. Lupascu, C. Quarti, G. Grancini, *JACS Au* **2021**, *2*, 136.

[25] L. J. Nugent, R. D. Baybarz, J. L. Burnett, J. L. Ryan, *J. Inorg. Nucl. Chem.* **1971**, *33*, 2503.

[26] X. Luo, G. Liang, J. Wang, X. Liu, K. Wu, *Chem. Sci.* **2019**, *10*, 2459.

[27] a) O. Meza, E. G. Villabona-Leal, L. A. Diaz-Torres, H. Desirena, J. L. Rodríguez-López, E. Pérez, *J. Phys. Chem. A* **2014**, *118*, 1390; b) S. Mei, J. Zhou, H. T. Sun, Y. Cai, L. D. Sun, D. Jin, C. H. Yan, *Adv. Sci.* **2021**, *8*, 2003325; c) T. Miyakawa, D. L. Dexter, *Phys. Rev. B* **1970**, *1*, 2961.

[28] P. Kratzer, J. Neugebauer, *Front. Chem.* **2019**, *7*, 106.

[29] a) P. E. Blöchl, *Phys. Rev. B* **1994**, *50*, 17953; b) M. Topsakal, R. M. Wentzcovitch, *Comput. Mater. Sci.* **2014**, *95*, 263.

[30] J. P. Perdew, K. Burke, M. Ernzerhof, *Phys. Rev. Lett.* **1996**, *77*, 3865.

[31] G. Meyer, *Prog. Solid State Chem.* **1982**, *14*, 141.

[32] P. A. Tanner, C. K. Duan, B. M. Cheng, *Spectrosc. Lett.* **2010**, *43*, 431.

[33] a) M. Ferbinteanu, A. Stroppa, M. Scarrozza, I. Humelnicu, D. Maftei, B. Frecus, F. Cimpoesu, *Inorg. Chem.* **2017**, *56*, 9474; b) A. Jaoul, G. Nocton, C. Clavaguéra, *ChemPhysChem* **2017**, *18*, 2688.

[34] a) C. J. Cramer, *Essentials of Computational Chemistry Theories and Models*, 2nd ed., Wiley, New York **2004**; b) P. G. Szalay, T. Müller, G. Gidofalvi, H. Lischka, R. Shepard, *Chem. Rev.* **2012**, *112*, 108.

[35] D. Aravena, M. Atanasov, F. Neese, *Inorg. Chem.* **2016**, *55*, 4457.

[36] D. Rappoport, *J. Chem. Phys.* **2021**, *155*, 124102.

[37] F. S. Richardson, M. F. Reid, J. J. Dallara, R. D. Smith, *J. Chem. Phys.* **1998**, *83*, 3813.

[38] Z. Li, M. Yang, J. S. Park, S. H. Wei, J. J. Berry, K. Zhu, *Chem. Mater.* **2016**, *28*, 284.

[39] R. D. Shannon, *Acta Crystallogr., Sect. A: Found. Adv.* **1976**, *32*, 751.

[40] J. Eng, E. Bucher, Z. Hu, T. Zheng, S. L. Gibbs, K. Chin, J. W. Gray, *Commun. Biol.* **2022**, *5*, 438.

[41] F. Chiappa, B. Frascella, G. P. Vigezzi, M. Moro, L. Diamanti, L. Gentile, P. Lago, N. Clementi, C. Signorelli, N. Mancini, A. Odone, *J. Hosp. Infect.* **2021**, *114*, 63.

[42] Y. Muramoto, M. Kimura, S. Nouda, *Semicond. Sci. Technol.* **2014**, *29*, 084004.